

Time-dependent multiconfiguration self-consistent-field method based on occupation restricted multiple active space model for multielectron dynamics in intense laser fields

Takeshi Sato* and Kenichi L. Ishikawa†

Photon Science Center, School of Engineering, The University of Tokyo,
7-3-1 Hongo, Bunkyo-ku, Tokyo 113-8656, Japan and

Department of Nuclear Engineering and Management, School of Engineering,
The University of Tokyo, 7-3-1 Hongo, Bunkyo-ku, Tokyo 113-8656, Japan

The time-dependent multiconfiguration self-consistent-field method based on the occupation-restricted multiple active space model is proposed (TD-ORMAS) for multielectron dynamics in intense laser fields. Extending the previously proposed time-dependent complete-active-space self-consistent-field method [TD-CASSCF; Phys. Rev. A, **88**, 023402 (2013)], which divides the occupied orbitals into core and active orbitals, the TD-ORMAS method *further* subdivides the active orbitals into an arbitrary number of subgroups, and poses the *occupation restriction* by giving the minimum and maximum number of electrons distributed in each subgroup. This enables highly flexible construction of the configuration interaction (CI) space, allowing a large-active-space simulation of dynamics, e.g., the core excitation or ionization. The equations of motion both for CI coefficients and spatial orbitals are derived based on the time-dependent variational principle, and an efficient algorithm is proposed to solve for the orbital time derivatives. In-depth descriptions of the computational implementation are given in a readily programmable manner. The numerical application to the one-dimensional lithium hydride cluster models demonstrates that the high flexibility of the TD-ORMAS framework allows for the cost-effective simulations of multielectron dynamics, by exploiting systematic series of approximations to the TD-CASSCF method.

I. INTRODUCTION

One of the main objectives of strong field physics and attosecond science is a direct measurement and control of electron motions in atoms and molecules [1]. The time-dependent Schrödinger equation (TDSE) provides the rigorous theoretical framework for investigating such electron dynamics [2–17]. However, direct real-space simulations of the TDSE to systems with more than two electrons are extremely difficult. To investigate multielectron dynamics in intense laser fields, the multiconfiguration time-dependent Hartree-Fock (MCTDHF) method has been developed [18–22], in which the time-dependent total wavefunction is given in the configuration interaction (CI) expansion,

$$\Psi(t) = \sum_{\mathbf{I}} \Phi_{\mathbf{I}}(t) C_{\mathbf{I}}(t), \quad (1)$$

where $\Phi_{\mathbf{I}}(t)$ is a Slater determinant built from a given number, n , of orbital functions $\{\phi_i(t)\}$. Both CI coefficients $\{C_{\mathbf{I}}\}$ and orbitals are simultaneously varied in time, which allows the use of considerably smaller number of orbitals than in the fixed orbital approach. This method, however, suffers from the exponential increase of the computational cost against the number of electrons N .

To circumvent this difficulty, we have recently proposed the time-dependent complete-active-space self-consistent-field (TD-CASSCF) method [23], which divides the orbitals into core and active orbitals. Simultaneously, the total electrons are classified into core and active electrons, $N = N_C + N_A$, and the CI expansion of Eq. (1) consists of all Slater

determinants including doubly occupied core orbitals. The flexible core-active classification enables compact yet accurate representation of dynamics according to the given physical situation. For example, in the presence of intense, long-wavelength laser pulses, the tightly bound electrons are expected to remain nonionized, while only weakly bound electrons ionize appreciably. The TD-CASSCF method is ideally suited to such situations, with tightly- and weakly-bound electrons treated as core and active, respectively.

The TD-CASSCF method is featured by the *fully* correlated description of the active electrons, by means of the *complete* CI expansion within the active orbitals. This guarantees that important properties of the rigorous MCTDHF method are preserved for the TD-CASSCF method including core orbitals [23]. However, the complete CI expansion still results in the exponential scaling of the computational cost albeit with respect to N_A , not to N . This causes an immediate difficulty when, e.g., the core ionization from tightly bound orbitals is of interest. In such situations, all electrons would have to be assigned as active. One should also recognize that, even for the dynamics dominated by chosen active electrons, the TD-CASSCF result with small number, n_A , of active orbitals is at best qualitative. Instead a sufficiently large number of orbitals, typically $n_A \geq 2N_A$ is required to obtain quantitatively, or even qualitatively correct descriptions. Again, the computational cost grows steeply against n_A for a fixed N_A , hindered large-active-space calculations. Clearly, the *non-complete* CI expansion is mandatory to have wider range of problems at hand.

An important step in this direction has been made in Ref. [24, 25], which divides the active orbitals into two subspaces, and allows variable distributions of electrons among the two subspaces. The method was applied to the one-dimensional model Hamiltonian [25], with the total wavefunc-

* Electronic mail: sato@atto.t.u-tokyo.ac.jp

† Electronic mail: ishikeni@atto.t.u-tokyo.ac.jp

tion given by the truncated CI expansion;

$$\Psi = \Phi_0 C_0 + \sum_{ia} \Phi_i^a C_i^a + \sum_{ijab} \Phi_{ij}^{ab} C_{ij}^{ab} + \cdots, \quad (2)$$

(time argument is omitted) where Φ_0 is the closed-shell Hartree-Fock determinant built from the $N_A/2$ spatial orbitals, Φ_i^a is the singly excited determinant with ϕ_i in Φ_0 replaced by ϕ_a in the second active subspace, Φ_{ij}^{ab} is the analogous doubly excited determinant, etc, truncated after a given order of excitations. Although this wavefunction converges to the complete-CI wavefunction with up to N_A -fold excitations included, the accuracy of this method is strongly system dependent, as discussed in the present work. In addition, the computational algorithm proposed in Ref. [25] involves severe bottleneck in increasing the order of excitations in Eq. (2). More flexible and efficient method is required to take full advantage of, and minimize the drawback of non-complete CI expansions.

In this work, we adopt the occupation-restricted multiple-active-space (ORMAS) model [26], originally developed for stationary electronic structure problems, as a highly flexible framework to construct non-complete CI spaces. On top of the core-active subspacing, the ORMAS method *further* divides the active orbitals into an arbitrary number of subgroups, and poses the *occupation restriction* through specifying the minimum and maximum numbers of electrons distributed in each subgroup. The ORMAS method has been applied [26, 27] both to fixed-orbital CI methods and to the multiconfiguration self-consistent-field (MCSCF) method, where not only CI coefficients but also the occupied orbitals are variationally optimized. Our interest is placed on the latter, in the context of the time-dependent non-stationary problems. Namely, we develop the time-dependent MCSCF method based on the ORMAS model, hereafter called the TD-ORMAS method.

This paper proceeds as follows. In Sec. II the ORMAS method is introduced in the rigorous second quantization formalism. Then in Sec. III, the equation of motion for the TD-ORMAS method is derived based on the time-dependent variational principle. The computational implementation is described in detail in Sec. IV. The performance of the TD-ORMAS method is assessed using one-dimensional multi-electron models in Sec. V. Finally, concluding remarks are given in Sec. VI. Appendix A–C, and D, respectively, describe further details of theory and implementation, and another numerical example. The Hartree atomic units are used throughout unless otherwise noted.

II. ANSATZ

In this section, we introduce the ORMAS method [26]. Since we consistently rely on the second quantization formalism in this work, we first briefly discuss the second quantized representation of the MCSCF wavefunction, followed by the rigorous definition of the ORMAS method. We consider a system with N_\uparrow (N_\downarrow) up (down) spin electrons, thus $N = N_\uparrow + N_\downarrow$ total electrons.

A. MCSCF wavefunctions in the second quantization

We define the set of N_b orthonormal spatial orbitals, $\{\phi_\mu\}$, assumed to span the spinless one-electron Hilbert space \mathcal{H} . In principle, \mathcal{H} consists of infinite number of orbitals, but in practice, the number of orbitals N_b is determined by the number of underlying basis functions, e.g., the number of spatial grid points in the finite difference approach. The one-electron complete-orthonormal basis is constructed by the direct product $\mathcal{H} \times \{\uparrow, \downarrow\}$, where \uparrow (\downarrow) represents the up (down) spin eigenfunction. This implies the spin-restricted treatment, using the same spatial orbitals for up and down spin orbitals. For each element of $\mathcal{H} \times \{\uparrow, \downarrow\}$, the Fermion creation (annihilation) operator $\hat{a}_{\mu\sigma}^\dagger$ ($\hat{a}_{\mu\sigma}$) is associated, with $\sigma \in \{\uparrow, \downarrow\}$.

The MCSCF wavefunction is based on the division of the full Hilbert space \mathcal{H} into occupied (\mathcal{P}) and virtual (\mathcal{Q}) orbital subspaces,

$$\mathcal{H} = \mathcal{P} + \mathcal{Q}, \quad (3)$$

where \mathcal{P} has n members called *occupied* orbitals, and remaining *virtual* orbitals form the \mathcal{Q} space:

$$\mathcal{P} = \{\phi_1, \phi_2, \cdots, \phi_n\}, \quad (4)$$

$$\mathcal{Q} = \{\phi_{n+1}, \phi_{n+2}, \cdots\}. \quad (5)$$

The determinant $\Phi_{\mathbf{I}}$ of Eq. (1) is built from the \mathcal{P} space orbitals only. The essence of the MCSCF method, both in the time-dependent and time-independent theories, is the variational separation of \mathcal{P} and \mathcal{Q} spaces; the CI problem is solved within the optimized \mathcal{P} space.

It is possible, and highly beneficial [23], to separate the occupied space into core (\mathcal{C}) and active (\mathcal{A}) subspaces,

$$\mathcal{P} = \mathcal{C} + \mathcal{A}, \quad (6)$$

where \mathcal{C} consists of n_C *core* orbitals, and \mathcal{A} of n_A *active* orbitals, with $n = n_C + n_A$:

$$\mathcal{C} = \{\phi_1, \phi_2, \cdots, \phi_{n_C}\}, \quad (7)$$

$$\mathcal{A} = \{\phi_{n_C+1}, \phi_{n_C+2}, \cdots, \phi_n\}. \quad (8)$$

At the same time, N electrons are classified into N_C core electrons and N_A active electrons, where

$$N_C = 2n_C, \quad (9)$$

$$N_A = N - N_C. \quad (10)$$

With these relations, the summation \mathbf{I} in Eq. (1) is taken over those Slater determinants including n_C doubly occupied core orbitals. Thus in the second quantization we write

$$|\Psi\rangle = \hat{\Phi}_C |\Psi_A\rangle, \quad |\Psi_A\rangle = \sum_{\mathbf{I}} |\mathbf{I}\rangle C_{\mathbf{I}}, \quad (11)$$

where $\hat{\Phi}_C \equiv \prod_{i \in \mathcal{C}} \hat{a}_{i\uparrow}^\dagger \hat{a}_{i\downarrow}^\dagger$ and $|\mathbf{I}\rangle$ represent the core and active parts of the determinant $\Phi_{\mathbf{I}}$ in Eq. (1), respectively, with

$$|\mathbf{I}\rangle = \hat{\mathbf{I}}|\rangle, \quad \hat{\mathbf{I}} = \prod_{\sigma} \prod_{t \in \mathcal{A}} (\hat{a}_{t\sigma}^\dagger)^{I_{t\sigma}}, \quad (12)$$

where $|\rangle$ represents the vacuum state, $I_{t\sigma} = \{0, 1\}$, and $\sum_{\sigma} \sum_{t \in \mathcal{A}} I_{t\sigma} = N_A$. In Eq. (11), the summation \mathbf{I} runs through the element of a CI space \mathcal{P} , which in general consists of a given set of active determinants $\{|\mathbf{I}\rangle\}$. Up to now, Eq. (11) represents the general MCSCF wavefunction (n_C can be zero). We separate the core part in Eq. (11) to maximally exploit the simplification due to the core wavefunction. In what follows, the term determinant denotes the active part $|\mathbf{I}\rangle$.

For later convenience, we introduce the following symbols:

$$\hat{\mathbf{I}}(\mathcal{A}') = \prod_{\sigma} \prod_{t \in \mathcal{A}'} (\hat{a}_{t\sigma}^{\dagger})^{I_{t\sigma}}, \quad (13)$$

$$[\mathcal{A}']^{N'} \equiv \left\{ \hat{\mathbf{I}}(\mathcal{A}'); \sum_{\sigma} \sum_{t \in \mathcal{A}'} I_{t\sigma} = N' \right\}, \quad (14)$$

where $\hat{\mathbf{I}}(\mathcal{A}')$ is the segment of $\hat{\mathbf{I}}$ for a given subset of active orbitals $\mathcal{A}' \subset \mathcal{A}$, and $[\mathcal{A}']^{N'}$ denotes the set of determinants constructed by distributing a given number, N' , of electrons among orbitals in \mathcal{A}' in all the possible ways.

B. ORMAS wavefunction

In the ORMAS model [26], the active orbital space \mathcal{A} is further subdivided into a given number, G , of subgroups;

$$\mathcal{A} = \mathcal{A}_1 + \mathcal{A}_2 + \cdots + \mathcal{A}_G, \quad (15)$$

$$\begin{aligned} \mathcal{A}_1 &= \{ \phi_1^{(1)}, \phi_2^{(1)}, \dots, \phi_{n_1}^{(1)} \}, \\ \mathcal{A}_2 &= \{ \phi_1^{(2)}, \phi_2^{(2)}, \dots, \phi_{n_2}^{(2)} \}, \\ &\dots \\ \mathcal{A}_G &= \{ \phi_1^{(G)}, \phi_2^{(G)}, \dots, \phi_{n_G}^{(G)} \}, \end{aligned} \quad (16)$$

with $n_A = \sum_{g=1}^G n_g$, and $\phi_j^{(g)} \equiv \phi_i$; $i = n_C + \sum_{g'=1}^{g-1} n_{g'} + j$. At the same time, the *occupation restriction* is posed through specifying the minimum and maximum numbers of electrons in each subgroup;

$$\begin{aligned} N_1^{\min} &\leq N_1 \leq N_1^{\max}, \\ N_2^{\min} &\leq N_2 \leq N_2^{\max}, \\ &\dots \\ N_G^{\min} &\leq N_G \leq N_G^{\max}, \end{aligned} \quad (17)$$

with

$$N_A = N_1 + N_2 + \cdots + N_G. \quad (18)$$

The boundaries of Eq. (17) determine the possible set of *occupation distributions* $\mathbf{d} = (N_1, N_2, \dots, N_G)$ which satisfies Eq. (18). Upon this active subspacing and occupation restriction, the ORMAS-CI space is constructed as

$$\mathcal{P}_{\text{ORMAS}} = \sum_{\mathbf{d}} \mathcal{P}(\mathbf{d}), \quad (19)$$

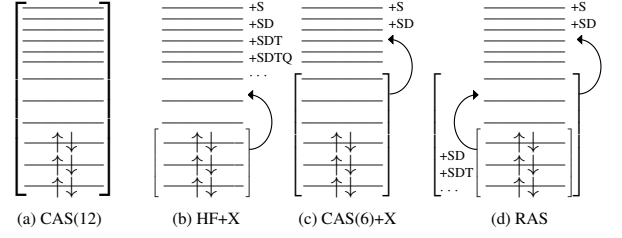


FIG. 1. Examples of the ORMAS-CI space for 6 active electrons and 12 active orbitals. (a) The CAS(12) space with no subdivision of active space. (b) The Hartree-Fock reference CI space with $(n_1, n_2) = (3, 9)$. (c) The CAS(6) reference CI space with $(n_1, n_2) = (6, 6)$. (d) An example of the RAS CI space with $(n_1, n_2, n_3) = (3, 3, 6)$. The first (lowest) group of orbitals, and also the union of first two groups in the case of RAS CI space, are bracketed. The straight up and down arrows represent electrons in the HF configuration, which are to be distributed according to the respective ORMAS restriction. The curved upward arrows image the excitations from one to the other subgroup. See text for more details.

$$\begin{aligned} \mathcal{P}(\mathbf{d}) &= [\mathcal{A}_1]^{N_1} [\mathcal{A}_2]^{N_2} \cdots [\mathcal{A}_G]^{N_G} \\ &= \left\{ \hat{\mathbf{I}} = \hat{\mathbf{I}}_1 \hat{\mathbf{I}}_2 \cdots \hat{\mathbf{I}}_G; \sum_{\sigma} \sum_{t \in \mathcal{A}_g} I_{t\sigma} = N_g, 1 \leq g \leq G \right\}, \end{aligned} \quad (20)$$

(21)

where $\hat{\mathbf{I}}_g \equiv \hat{\mathbf{I}}(\mathcal{A}_g)$. The ORMAS-CI space is given by the direct sum [Eq. (19)] of disjoint CI spaces $\mathcal{P}(\mathbf{d})$ for all the allowed distributions $\{\mathbf{d} = (N_1, N_2, \dots, N_G)\}$, where $\mathcal{P}(\mathbf{d})$ is the direct product space [Eq. (20)], consisting of determinants built by distributing N_1 electrons in the subgroup \mathcal{A}_1 , N_2 electrons in \mathcal{A}_2 , \dots , and N_G electrons in \mathcal{A}_G , in all the possible ways [Eq. (21)].

Here we give a few examples of the ORMAS-CI spaces:

- 1) No subdivision of \mathcal{A} ($G = 1, N_{\min}^1 = N_{\max}^1 = N_A$) gives the complete CI space [Fig. 1 (a)];

$$\mathcal{P}_{\text{CAS}} = [\mathcal{A}]^{N_A}. \quad (22)$$

The TD-CASSCF method [23] is based on this CI space. In this work, the TD-CASSCF method with n_A active orbitals is simply denoted as CAS(n_A).

- 2) As shown in Fig. 1 (b) and (c), dividing \mathcal{A} into two subgroups ($G = 2$), and restricting the occupation by $N_A - L \leq N_1 \leq N_A, 0 \leq N_2 \leq L$, for a given L generates the CI space including all the determinants built from the first (lowest in Fig. 1) active orbitals (*reference CI space*), and those configurations generated by single, double, triples, \dots , and up to L -fold excitations from the reference to the second subgroup. Especially, we focus on the following two schemes;

Hartree-Fock reference CI space: With $n_1 = N_A/2$, the CI space includes the Hartree-Fock reference determinant plus excitations from the reference to the second subgroup. The corresponding TD-ORMAS method is denoted as HF+X for brevity, with X = S, SD, SDT, and

so on, indicating the inclusion of only single, single and double, up to triple excitations, etc. The first quantized expression is given by Eq. (2), which is pictorially explained in Fig. 1 (b)

CAS(N_A) reference CI space: With $n_1 = N_A$, the CI space consists of all the determinants built from the first N_A active orbitals [CAS(N_A) reference], plus excitations from the reference to the second subgroup. The corresponding TD-ORMAS method is denoted as CAS(N_A)+X. An example is given in Fig. 1 (c)

- 3) Another important example, shown in Fig. 1 (d), is the so-called *restricted active space* (RAS) model proposed by Olsen *et al* [28], which divides \mathcal{A} into three subgroups ($G = 3$), and restricts the occupation by setting the maximum number of holes M_{hole} in \mathcal{A}_1 and the maximum number of electrons M_{elec} in \mathcal{A}_3 , while N_2 is unconstrained. In the ORMAS notation, this corresponds to the following boundaries;

$$N_A - M_{\text{hole}} \leq N_1 \leq N_A, \quad 0 \leq N_3 \leq M_{\text{elec}}. \quad (23)$$

The RAS scheme allows excitations (1) from the first subgroup into the second, and (2) from the union of first two subgroups into the third, up to different maximum ranks, M_{hole} and M_{elec} for (1) and (2), respectively. Figure 1 (d) shows a special case with $N_A = 2n_1$, for which $M_{\text{elec}} \leq M_{\text{hole}}$ should hold.

Note that the ‘‘TD-RASSCF’’ method proposed in Ref. [25] uses the second type of CI spaces, but not based on the RAS scheme of Ref. [28]. To avoid confusion and for consistency with the terminology widely used in the stationary electronic structure theory, we refer to the latter method as RAS, which includes the method of Ref. [25] as a special case. The ORMAS framework can be used to construct a variety of other CI spaces as summarized in Ref. [26], allowing a tailored approximation for a given problem. In Sec. V we discuss the physical significance and computational (dis)advantages of these models with numerical applications.

III. TD-ORMAS METHOD

A. Time-dependent variational method in the second quantization

We first review the general EOMs for CI coefficients and orbitals [Eq. (32) and (33) below] derived in our previous work [23]. The same equations have been the basis of Refs. [24, 25, 29]. Based on the time-dependent variational principle [30–32], the following action integral S ,

$$S = \int dt \langle \Psi | \hat{H} - i \frac{\partial}{\partial t} | \Psi \rangle, \quad (24)$$

is required to be stationary, i.e., $\delta S = 0$, with

$$\delta S = \delta \langle \Psi | \hat{H} | \Psi \rangle - i \left(\langle \delta \Psi | \frac{\partial \Psi}{\partial t} \rangle - \langle \frac{\partial \Psi}{\partial t} | \delta \Psi \rangle \right). \quad (25)$$

Here \hat{H} is the spin-free second-quantized Hamiltonian,

$$\hat{H} = \sum_{\mu\nu} h_{\nu}^{\mu} \hat{E}_{\nu}^{\mu} + \frac{1}{2} \sum_{\mu\nu\lambda\gamma} g_{\nu\gamma}^{\mu\lambda} \hat{E}_{\nu\gamma}^{\mu\lambda}, \quad (26)$$

with $\hat{E}_{\nu}^{\mu} = \sum_{\sigma} \hat{a}_{\mu\sigma}^{\dagger} \hat{a}_{\nu\sigma}$, $\hat{E}_{\nu\gamma}^{\mu\lambda} = \sum_{\sigma\tau} \hat{a}_{\mu\sigma}^{\dagger} \hat{a}_{\lambda\tau}^{\dagger} \hat{a}_{\gamma\tau} \hat{a}_{\nu\sigma}$, and

$$h_{\nu}^{\mu} = \int d\mathbf{r} \phi_{\mu}^*(\mathbf{r}) h(\mathbf{r}, \nabla_{\mathbf{r}}) \phi_{\nu}(\mathbf{r}), \quad (27)$$

$$g_{\nu\gamma}^{\mu\lambda} = \iint d\mathbf{r}_1 d\mathbf{r}_2 \frac{\phi_{\mu}^*(\mathbf{r}_1) \phi_{\nu}(\mathbf{r}_1) \phi_{\lambda}^*(\mathbf{r}_2) \phi_{\gamma}(\mathbf{r}_2)}{|\mathbf{r}_1 - \mathbf{r}_2|}, \quad (28)$$

where the one-electron matrix element h_{ν}^{μ} consists of kinetic, nucleus-electron, and external laser terms. The orthonormality-conserving representation of variations and time derivatives of orbitals are given [23, 29] by

$$\delta \phi_p = \sum_{\mu} \phi_{\mu} \Delta_p^{\mu}, \quad \Delta_p^{\mu} = \langle \phi_{\mu} | \delta \phi_p \rangle, \quad (29)$$

$$\frac{\partial \phi_p}{\partial t} = \sum_{\mu} \phi_{\mu} X_p^{\mu}, \quad X_p^{\mu} = \langle \phi_{\mu} | \frac{\partial \phi_p}{\partial t} \rangle, \quad (30)$$

in terms of anti-Hermitian transformation matrices Δ and X . Note that in Ref. [23], the Hermitian matrix $R \equiv iX$ was used as the working variable. We change notation for a better transferability between real and imaginary time equations as discussed in appendix C. Using these matrices, the variation $\delta \Psi$ and the time derivative $\dot{\Psi} \equiv \partial \Psi / \partial t$ of the total wavefunction are compactly given [23] by;

$$|\delta \Psi\rangle = \hat{\Phi}_C \sum_{\mathbf{I}} |\mathbf{I}\rangle \delta C_{\mathbf{I}} + \hat{\Delta} |\Psi\rangle \quad (31a)$$

$$|\dot{\Psi}\rangle = \hat{\Phi}_C \sum_{\mathbf{I}} |\mathbf{I}\rangle \dot{C}_{\mathbf{I}} + \hat{X} |\Psi\rangle, \quad (31b)$$

where $\hat{\Delta} = \sum_{\mu\nu} \Delta_{\nu}^{\mu} \hat{E}_{\nu}^{\mu}$, $\hat{X} = \sum_{\mu\nu} X_{\nu}^{\mu} \hat{E}_{\nu}^{\mu}$. Inserting Eqs. (31) into Eq. (25) and requiring $\delta S / \delta C_{\mathbf{I}} = 0$, $\delta S / \delta \Delta_{\nu}^{\mu} = 0$, gives [23]

$$\dot{C}_{\mathbf{I}} = -i \langle \mathbf{I} | \hat{\Phi}_C^{\dagger} \hat{H} | \Psi \rangle - \langle \mathbf{I} | \hat{\Phi}_C^{\dagger} \hat{X} | \Psi \rangle, \quad (32)$$

$$\langle \Psi | \hat{E}_{\nu}^{\mu} \hat{Q} \hat{X} - \hat{X} \hat{Q} \hat{E}_{\nu}^{\mu} | \Psi \rangle = -i \langle \Psi | \hat{E}_{\nu}^{\mu} \hat{Q} \hat{H} - \hat{H} \hat{Q} \hat{E}_{\nu}^{\mu} | \Psi \rangle. \quad (33)$$

Hereafter, we use notations \hat{P} and \hat{Q} (with upright typeface) to denote the configuration projector onto and against the CI space P , respectively; $\hat{P} = \sum_{\mathbf{I}} |\mathbf{I}\rangle \langle \mathbf{I}|$, and $\hat{Q} = \hat{1} - \hat{P}$. Equations (32) and (33) are the general EOMs for CI coefficients and orbitals, respectively, valid for MCSCF wavefunctions with arbitrary CI spaces P .

Equation (33) suggests that the set of orbital rotations $\{\hat{E}_{\nu}^{\mu}\}$ can be classified into the following disjoint categories:

- (A) *Redundant.* Both $\hat{E}_{\nu}^{\mu} |\Psi\rangle$ and $\hat{E}_{\mu}^{\nu} |\Psi\rangle$ lie inside P or vanish. In this case, Eq. (33) reduces to an identity (thus called *redundant*), and X_{ν}^{μ} may be arbitrary anti-Hermitian matrix elements [18]:

$$X_{\nu}^{\mu} = \langle \phi_{\mu} | \hat{\theta}(t) | \phi_{\nu} \rangle, \quad \hat{\theta}^{\dagger}(t) = -\hat{\theta}(t). \quad (34)$$

(B) *Non-redundant uncoupled.* At least one of $\hat{E}_\nu^\mu|\Psi\rangle$ and $\hat{E}_\mu^\nu|\Psi\rangle$ do not vanish, and $\hat{E}_\nu^\mu|\Psi\rangle$ and $\hat{E}_\mu^\nu|\Psi\rangle$ lie, if non-vanishing, outside P. Such rotations do not contribute to the CI equations, Eq. (32) (thus called *uncoupled*). In this case, Eq. (33) reduces to a simpler expression [23],

$$\langle\Psi|[\hat{E}_\nu^\mu, \hat{E}_\lambda^\gamma]|\Psi\rangle X_\lambda^\gamma = -i\langle\Psi|[\hat{E}_\nu^\mu, \hat{H}]|\Psi\rangle. \quad (35)$$

(C) *Non-redundant coupled.* Either $\hat{E}_\nu^\mu|\Psi\rangle$ or $\hat{E}_\mu^\nu|\Psi\rangle$ lies across P and Q. Such rotations do contribute to both the CI and orbital EOMs (thus called *coupled*). In this case, one needs to directly work with Eq. (33).

B. Analyses of orbital rotations in the ORMAS wavefunction

In what follows, we use orbital indices $\{i, j, k\}$ for core (C), $\{t, u, v, w, x, y\}$ for active (A), $\{p, q, r, s\}$ for occupied (P), $\{a, b, c\}$ for virtual (Q), and $\{\mu, \nu, \lambda, \gamma, \delta\}$ for general (H) orbitals. The whole set of orbital rotations within the \mathcal{H} space is categorized as follows:

$$\{\hat{E}_\nu^\mu\} = \{\hat{E}_j^i, \hat{E}_t^i, \hat{E}_t^t, \hat{E}_u^t, \hat{E}_a^p, \hat{E}_p^a, \hat{E}_b^a\}. \quad (36)$$

Reference [23] identifies the core-core and virtual-virtual rotations $\{\hat{E}_j^i, \hat{E}_b^a\}$ as redundant, and core-active and occupied-virtual rotations $\{\hat{E}_t^i, \hat{E}_t^t, \hat{E}_p^a, \hat{E}_a^p\}$ as non-redundant uncoupled, for the CASSCF wavefunction. This conclusion is valid for general CI space P, since the derivation of Ref. [23] makes no use of the internal structure of the active space (complete or non-complete) for these parameters. Furthermore, for the same reason, the final expression of relevant time derivative terms $\{X_i^t, X_t^i, X_p^a\}$ of TD-CASSCF method applies to general MCSCF wavefunctions with no modifications.

Left unexplored above is the active-active rotations $\{\hat{E}_u^t\}$, which we analyze as follows. First, active intra-group rotations $\{E_u^t; \phi_t, \phi_u \in \mathcal{A}_g\}$ are redundant, since such rotations do not change the occupation distribution, and the expansion of Eq. (20) is complete for a given distribution; for every $|\mathbf{I}\rangle \in \mathcal{P}(\mathbf{d}) \subset \mathcal{P}$, $\hat{E}_u^t|\mathbf{I}\rangle \in \mathcal{P}(\mathbf{d}) \subset \mathcal{P}$, thus $\hat{E}_u^t|\Psi\rangle \in \mathcal{P}$. Next, active inter-group rotations $\{E_u^t; \phi_t \in \mathcal{A}_g, \phi_u \in \mathcal{A}_{g'}, g \neq g'\}$ are, in general, non-redundant coupled. This is understood by considering the simplest example of Fig. 1 (b) with, e.g., single and double excitations from the first into the second subgroup included. In this example, the CI space is given by $\mathcal{P} = \mathcal{P}(6, 0) + \mathcal{P}(5, 1) + \mathcal{P}(4, 2)$. Then if $|\mathbf{I}\rangle \in \mathcal{P}(6, 0)$, then $\hat{E}_u^t|\mathbf{I}\rangle \in \mathcal{P}(5, 1) \subset \mathcal{P}$ where ϕ_u and ϕ_t belong to the first and second subgroups, respectively. However for the same rotation, if $|\mathbf{I}\rangle \in \mathcal{P}(4, 2)$, then $\hat{E}_u^t|\mathbf{I}\rangle \in \mathcal{P}(3, 3) \subset \mathcal{Q}$, thus $\hat{E}_u^t|\Psi\rangle$ lies across P and Q. See Ref. [24] for a similar discussion.

C. Final expression of TD-ORMAS orbital equations of motion

As pointed out in the previous subsection, the equations for the CI coefficients and orbitals except the terms $\{X_u^t\}$ are independent of the active space structure. Thus we write down

the final expression of EOMs by referring to the TD-CASSCF formulae [23], first for orbitals in this subsection and for CI coefficients in the next subsection, with active-active terms $\{X_u^t\}$ left unspecified until Sec. III E. The orbital EOMs are given by

$$|\dot{\phi}_p\rangle = -i\hat{Q}\hat{F}_p|\phi_p\rangle + \sum_q |\phi_q\rangle X_p^q, \quad (37)$$

where \hat{Q} is the orbital projector onto the Q space;

$$\hat{Q} \equiv \sum_a |\phi_a\rangle\langle\phi_a| = \hat{1} - \sum_p |\phi_p\rangle\langle\phi_p|, \quad (38)$$

which prevents the explicit use of virtual orbitals [18], and

$$\hat{F}_i|\phi_i\rangle = \hat{f}|\phi_i\rangle + \sum_{tu} D_u^t \hat{G}_u^t |\phi_i\rangle, \quad (39a)$$

$$\hat{F}_t|\phi_t\rangle = \hat{f}|\phi_t\rangle + \sum_{uvw} \hat{W}_w^v |\phi_u\rangle P_{xv}^{uw} (D^{-1})_t^x, \quad (39b)$$

where $D_u^t \equiv \langle\Psi_A|\hat{E}_t^u|\Psi_A\rangle$ and $P_{uv}^{tw} \equiv \langle\Psi_A|\hat{E}_{tv}^{uw}|\Psi_A\rangle$ are one- and two-electron reduced density matrix (RDM) elements, respectively, defined within the active space, and

$$\hat{f}|\phi_p\rangle = \hat{h}|\phi_p\rangle + 2 \sum_j \hat{G}_j^j |\phi_p\rangle, \quad (40)$$

$$\hat{G}_q^p |\phi_r\rangle = \hat{W}_q^p |\phi_r\rangle - \frac{1}{2} \hat{W}_r^p |\phi_q\rangle, \quad (41)$$

$$W_q^p(\mathbf{r}_1) = \int d\mathbf{r}_2 \frac{\phi_p^*(\mathbf{r}_2)\phi_q(\mathbf{r}_2)}{|\mathbf{r}_1 - \mathbf{r}_2|}. \quad (42)$$

The core-active term X_i^t is given [23] by the solution of the following matrix equation:

$$(2\delta_u^t - D_u^t)X_i^u = -iB_i^t, \quad (43)$$

and $X_t^i = -X_i^{t*}$, where

$$B_i^t \equiv \langle\Psi|[\hat{E}_t^i, \hat{H}]|\Psi\rangle = 2F_i^t - D_u^t F_u^{i*}, \quad (44)$$

$$B_u^t \equiv \langle\Psi|[\hat{E}_t^u, \hat{H}]|\Psi\rangle = \sum_v (F_v^t D_u^v - D_v^t F_v^{u*}), \quad (45)$$

are the so called Brillouin matrix elements used in the stationary MCSCF methods, and

$$F_q^p = \langle\phi_p|\hat{F}_q|\phi_q\rangle. \quad (46)$$

With no core orbitals, the core fock operator of Eq. (40) reduces to the bare one-electron operator \hat{h} , whereas if core orbitals are classified into frozen (fixed in time) and dynamical (allowed to vary in time) core orbitals [23], the range of core indices i, j should be restricted to dynamical cores in all equations in this section, with the operator \hat{h} in Eq. (40) replaced with \hat{h}^{FC} given by

$$\hat{h}^{\text{FC}}(t) = \hat{h}(t) + 2 \sum_k^{\text{FC}} \hat{G}_k^k(0), \quad (47)$$

where the summation k is restricted within the frozen-core orbitals. Equation (47) emphasizes the fact that the (direct and exchange) two-electron contributions from the frozen-core electrons, $\hat{G}_k^k(0) \equiv \hat{G}_k^k(t=0)$ are time-independent.

D. Final expression of TD-ORMAS CI equations of motion

The CI equation is given as follows [23];

$$\dot{\mathbf{C}} = -i(\mathbf{I}|\hat{H}_A - E_A\hat{1}|\Psi_A) - \langle \mathbf{I}|\hat{X}|\Psi_A \rangle, \quad (48)$$

$$\hat{H}_A = \sum_{tu} f_u^t \hat{E}_u^t + \frac{1}{2} \sum_{tuvw} g_{uv}^{tv} \hat{E}_{uv}^{tv}, \quad (49)$$

where $\hat{1}$ is a unit operator, $E_A \equiv \langle \Psi_A | \hat{H}_A | \Psi_A \rangle$, and

$$f_u^t = \langle \phi_t | \cdot \hat{f} | \phi_u \rangle, \quad (50)$$

$$g_{uv}^{tv} = \langle \phi_t | \cdot \hat{W}_w^v | \phi_u \rangle. \quad (51)$$

In Eq. (48), we make, without loss of generality, a particular phase choice so that $\langle \Psi | \dot{\Psi} \rangle = 0$. Another, more common choice of the phase $i\langle \Psi | \dot{\Psi} \rangle = \langle \Psi | \hat{H} | \Psi \rangle$ replaces the operator $\hat{H}_A - E_A\hat{1}$ in Eq. (48) with $\hat{H}_A + E_C\hat{1}$ where $E_C = 2\sum_j f_j^j$. These approaches are mathematically equivalent, but the former improves the stability of both real and imaginary propagations [23]. The separation of the core wavefunction in Eq. (11) allows to formulate the CI equation as the effective N_A -electron problem [Eq. (48)], rather than that of the total N electrons [Eq. (32)].

E. Active inter-group contributions

Now we turn to the active inter-group rotations $\{E_u^t\}$ to derive the equation for $\{X_u^t\}$. Let us re-emphasize that Eqs. (37) and (48) are valid irrespective of the active space structure. The equation to be solved for $\{X_u^t\}$, derived in this subsection, thus finalizes our derivation of the TD-ORMAS method.

Although Eq. (33) is useful for the formal discussion as made in Sec. III A, it does not fully take into account the anti-Hermiticity of matrices Δ and X . Thus, instead of starting from Eq. (33), we directly work with real and imaginary parts of Δ and X ;

$$\Delta_u^t = \Delta_{tu}^R + i\Delta_{tu}^I, \quad (52)$$

$$X_u^t = X_{tu}^R + iX_{tu}^I. \quad (53)$$

Here Δ^R, X^R are anti-symmetric, and Δ^I, X^I are symmetric. The active inter-group parts of operators $\hat{\Delta}$ and \hat{X} are now expressed as

$$\hat{\Delta} = \sum'_{t>u} \left(\Delta_{tu}^R \hat{E}_{tu}^- + i\Delta_{tu}^I \hat{E}_{tu}^+ \right), \quad (54)$$

$$\hat{X} = \sum'_{t>u} \left(X_{tu}^R \hat{E}_{tu}^- + iX_{tu}^I \hat{E}_{tu}^+ \right), \quad (55)$$

where $\hat{E}_{tu}^\mp = \hat{E}_u^t \mp \hat{E}_t^u$. The primed summations in these equations are taken over active inter-group rotations, which amounts to N_{rot} nonequivalent rotations with

$$N_{\text{rot}} = \sum_{g>g'}^G n_g n_{g'}. \quad (56)$$

Inserting Eqs. (54) and (55) into Eq. (31), and requiring that δS of Eq. (25) vanishes for Δ_{tu}^R and Δ_{tu}^I separately, after straightforward rearranging of terms, we have

$$\sum'_{v>w} (A_{tu,vw}^{--} X_{vw}^R + A_{tu,vw}^{-+} X_{vw}^I) = b_{tu}^-, \quad (57a)$$

$$\sum'_{v>w} (A_{tu,vw}^{+-} X_{vw}^R + A_{tu,vw}^{++} X_{vw}^I) = b_{tu}^+, \quad (57b)$$

where

$$A_{tu,vw}^{\mp\mp} = \pm \text{Im} \langle \Psi_A | \hat{E}_{tu}^\mp \hat{Q} \hat{E}_{vw}^\mp | \Psi_A \rangle, \quad (58)$$

$$A_{tu,vw}^{\mp\pm} = \pm \text{Re} \langle \Psi_A | \hat{E}_{tu}^\mp \hat{Q} \hat{E}_{vw}^\pm | \Psi_A \rangle, \quad (59)$$

$$b_{tu}^- = -\text{Re} \langle \Psi_A | \hat{E}_{tu}^- \hat{Q} \hat{H}_A | \Psi_A \rangle, \quad (60)$$

$$b_{tu}^+ = +\text{Im} \langle \Psi_A | \hat{E}_{tu}^+ \hat{Q} \hat{H}_A | \Psi_A \rangle. \quad (61)$$

Equation (57) is the desired formulae for the active inter-group contributions to the orbital time derivative. Although our main focus is on the use of the ORMAS model, this equation is in fact valid for the general MCSCF wavefunction with arbitrary CI spaces \mathbf{P} since it is equivalent to Eq. (33), the general equation. However, without a systematic construction of CI spaces, in general, all pairs of active orbitals with $N_{\text{rot}} = n_A(n_A + 1)/2$, instead of Eq. (56), have to be included, with no control of (non-) redundancy of active-active rotations. The advantage of the TD-ORMAS method is that it can limit the application of Eq. (57) to non-redundant, inter-group pairs only. This improves both the efficiency and stability of the temporal propagation.

IV. IMPLEMENTATION

This section describes our implementation of the TD-ORMAS method. Input parameters required are the number of core (n_C) and active (n_A) orbitals, the number of active subgroups G , and the size and occupation boundaries of each subgroup;

$$\mathbf{n} = (n_1, n_2, \dots, n_G), \quad (62)$$

$$N_{\text{min}} = (N_1^{\text{min}}, N_2^{\text{min}}, \dots, N_G^{\text{min}}), \quad (63)$$

$$N_{\text{max}} = (N_1^{\text{max}}, N_2^{\text{max}}, \dots, N_G^{\text{max}}). \quad (64)$$

Our code first checks if the given input is a sensible one. Thereafter, the possible set of occupation distributions \mathbf{d} and the information of the CI space are automatically generated using the algorithm of Ref. [26].

Note that (some of) the inter-group rotations may turn out to be redundant, e.g., due to the symmetry. Our code removes such redundant rotations from Eqs. (57), if detected in advance. It can also happen that some inter-group rotations are identified as non-redundant uncoupled, e.g., when a subgroup \mathcal{A}_g has a fixed occupation $N_g^{\text{min}} = N_g^{\text{max}}$, which makes all rotations involving an orbital in \mathcal{A}_g and the other outside \mathcal{A}_g non-redundant uncoupled. For such cases, we still use the general equation [Eq. (57)], since the reduction to simpler expression [Eq. (35)] leads to no significant computational gains.

Any type of propagators require the evaluation of time derivatives of variables $\{\hat{C}_I, \phi_p\}$ from the set of variables $\{C_I, \phi_p\}$. This proceeds as follows;

- (1) Compute the active space RDMs $\{D_u^t, P_{uv}^{tv}\}$ from the current CI coefficients. We use the algorithm of Ref. [33] to efficiently handle the “coupling coefficients” $\langle \mathbf{I} | \hat{E}_u^t \hat{E}_w^v | \mathbf{I}' \rangle$ in non-complete CI spaces.
- (2) Compute \mathcal{Q} -space contributions to the orbital derivatives [the first term of Eq. (37)] from the current orbitals and RDMs obtained in the step (1). This is done by first evaluating the one-electron operator acting on occupied orbitals $\hat{h}|\phi_p\rangle$ and meanfield operators \hat{W}_q^p defined in Eq. (42), from which $\hat{f}|\phi_p\rangle$ and $\hat{G}_u^t|\phi_i\rangle$ are evaluated according to Eqs. (40) and (41), respectively, and the right-hand sides of Eqs. (39a) and (39b) are accumulated. To avoid the possible (near) singularity of inverse 1RDM in Eq. (39b), the eigenvalues $\{d_i\}$ of D are regularized as $1/d_i \rightarrow d_i/(d_i^2 + \delta^2)$, where δ is a small positive number.
- (3) Compute the one- and two-electron Hamiltonian elements, f_u^t and g_{uv}^{tv} entering Eq. (49) by performing the inner products of Eqs. (50) and (51), using $\hat{f}|\phi_t\rangle$ and \hat{W}_q^p obtained in the step (2).
- (4) Compute the Brillouin matrix elements B_q^p entering Eqs. (43) and (A4) by performing the inner products of Eq. (46), using $\hat{F}_p|\phi_p\rangle$ obtained in the step (2).
- (5) Compute the direct Hamiltonian contribution to the CI derivative [the first term of Eq. (48)] from the matrix elements f_u^t, g_{uv}^{tv} evaluated in the step (3) and the current CI coefficients. The algorithm of Ref. [33] is also used here.
- (6) Compute the core-active contributions to the orbital derivative $\{X_i^t, X_i^i\}$ by solving Eq. (43). The regularization method given above is applied to the matrix $2\mathbf{1} - D$, where $\mathbf{1}$ is a $n_A \times n_A$ identity matrix.
- (7) Compute the active inter-group contributions to the orbital derivative $\{X_u^t\}$. First, the matrix elements of Eqs. (58)-(61) are evaluated by the method described in Appendix A. Then Eq. (57) is formulated as a real-valued matrix equation with the dimension $2N_{\text{rot}}$;

$$\mathbf{A}\mathbf{x} = \mathbf{b}, \quad (65)$$

where $\mathbf{A} \equiv ((A^{--}, A^{+-})^t, (A^{-+}, A^{++})^t)$, $\mathbf{b} \equiv (b^-, b^+)^t$, and \mathbf{x} is the solution vector whose first and last N_{rot} elements being the real and imaginary parts of X , respectively. Here the matrix \mathbf{A} is anti-symmetric for a real time derivative [Eqs. (58) and (59)], and symmetric for an imaginary time derivative [Eqs. (C3) and (C4)]. This equation is solved by the singular value decomposition of the coefficient matrix \mathbf{A} , with its singular values being regularized by the same procedure as used in the steps (2) and (6).

- (8) Add in the completed \mathcal{P} -space orbital derivative matrix $\{X_q^p\}$ both to the orbital equation [Eqs. (37)] and to the CI equation [Eq. (48)].

For the full MCTDHF method, steps (1)-(3), (5) [and (8) if $\hat{\theta} \neq 0$ in Eq. (34)] complete the evaluation of time derivatives. The TD-CASSCF method requires steps (1)-(6) and (8). For more general cases, all steps have to be executed. See Ref. [23] for more detailed explanation of these steps except (7). The efficient algorithm given in Appendix A allows the step (7) to be performed with a very small computational cost.

The above-described procedures are used both for real-time propagations and imaginary-time propagations (to obtain the stationary state). For the latter case, each propagation is followed by the normalization of CI coefficients and the Schmidt orthonormalization of orbitals. One should be careful in transforming the real-time EOMs into the imaginary-time ones in the case of non-complete CI spaces. Appendix C explicitly gives the equations appropriate for the imaginary-time propagation.

V. APPLICATIONS

In this section, we apply the TD-ORMAS method to the one-dimensional (1D) model systems. The 1D multielectron models have served as convenient but reliable testing ground for assessing new theoretical methods [18, 23–25, 34–39]. By doing this we demonstrate the flexibility of the ORMAS framework, and discuss (dis)advantages of various options of active spaces. The 1D model Hamiltonian for N electrons in the potential of M fixed nuclei interacting with an external laser electric field $E(t)$ is taken as

$$H = \sum_i^N \left\{ -\frac{1}{2} \frac{\partial^2}{\partial x_i^2} - \sum_a^M \frac{Z_a}{\sqrt{(x_i - X_a)^2 + c}} - E(t)x_i \right\} + \sum_{i>j}^N \frac{1}{\sqrt{(x_i - x_j)^2 + d}}, \quad (66)$$

where x_i is the position of the i -th electron, $\{X_a\}$ and $\{Z_a\}$ are the positions and charges of nuclei, and $c = 0.5$ and $d = 1$

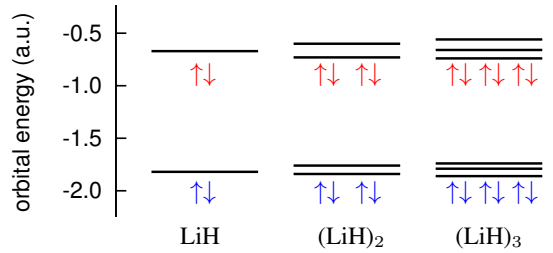


FIG. 2. Hartree-Fock orbital energy levels of 1D-LiH clusters. Numerical values obtained for $(\text{LiH})_3$ are -1.860, -1.794, -1.742, -0.747, -0.661, and -0.565. Those for LiH (-1.824 and -0.674) and $(\text{LiH})_2$ (-1.848, -1.767, -0.728, and -0.599) are taken from Ref. [23]. Red and blue arrows indicate electrons occupying the weakly and deeply bound orbitals, respectively.

[23] adjust the soft Coulomb operators of electron-nuclear and electron-electron interactions, respectively. The electron-laser interaction is included within the dipole approximation and in the length gauge. Note that the result is gauge invariant [23, 25]. The redundant orbital rotations of Eq. (34) are fixed as $\hat{\theta} = 0$, and the regularization parameter δ introduced in Sec. IV is taken to be sufficiently small (typically $\delta = 10^{-10}$). The orbital EOMs are discretized on equidistant grid points with spacing $\Delta x = 0.4$ and box size $|x| < 600$. Further computational details are the same as in Ref. [23].

Specifically, we investigate 1D lithium hydride (LiH) cluster models, 1D-(LiH) $_m$ [23], with $m = 1, 2, 3$. We consider the collinear configuration, LiH-LiH- \cdots (nuclear charges 3131 \cdots), with interatomic LiH distance 2.3 and intermolecular H-Li distance 3.5 as optimized for (LiH) $_2$ [23]. Figure 2 shows the ground-state Hartree-Fock orbital energies. As shown in the figure, the electronic structure of (LiH) $_m$ consists of m tightly bound orbitals (with $2m$ electrons) and m weakly bound orbitals (with $2m$ electrons). This is the consequence of the strong bonding interaction within LiH and the weak intermolecular interaction between LiH molecules. We have previously found the following observations [23] for $m = 1, 2$;

- 1) The lowest $n_C = m$ orbitals can be treated as core in a very good approximation: The TD-CASSCF method, with only the upper $N_A = 2m$ electrons treated as active, closely reproduces the full MCTDHF results.
- 2) At least $n_A = 2N_A$ orbitals are required for N_A active electrons to obtain the convergent results for, e.g., the temporal evolution of the dipole moment and ionization yields in the presence of an intense laser field.

As a preliminary to the present work, we confirmed that the latter conclusion is valid also for (LiH) $_3$; successive TD-CASSCF calculations with $N_A = 6$ and increasing n_A reached the convergence at $n_A = 12$ for the above observables. We could not perform the full MCTDHF calculation with $n = n_C + n_A = 15$ orbitals and $N = N_C + N_A = 12$ electrons due to the large CI dimension (more than 25 million determinants) which exceeds the capability of our present computational code. However, one reasonably expects a similar accuracy for TD-CASSCF descriptions of (LiH) $_3$ as for those of smaller systems. In this work, therefore, we use the TD-CASSCF method with $N_A = 2m$ active electrons and $n_A = 2N_A$ active orbitals, abbreviated by CAS($2N_A$), as a standard.

Table I shows the ground state properties of 1D-(LiH) $_3$ obtained with various methods, grouped according to the type of underlying CI spaces discussed in Sec. II B. The rigorous definitions of these methods are given below in Secs. V A-V C. At this point, we mention that these classes of methods provide different series of approximations, whose accuracy can be improved systematically until final convergence to the CAS($2N_A$) description. Table I demonstrates such a systematic improvement for each class of methods, where the total energy and the dipole moment of the ground state are converged to the CAS($2N_A$) values to four and three decimal

TABLE I. Ground state properties of 1D-(LiH) $_3$ model. The number of active orbitals n_A , the number of determinants N_{det} , the total energy E , and the dipole moment $\langle x \rangle$ are shown for various methods.

Method	n_A	N_{det}	E	$\langle x \rangle$
HF reference CI wavefunctions				
HF	3	1	-21.2125	-3.128
+S	6	19	-21.2300	-3.214
+SD	12	1,000	-21.2636	-3.336
+SDT	12	7,000	-21.2647	-3.352
+SDTQ	12	23,200	-21.2653	-3.356
CAS(6) reference CI wavefunctions				
CAS(6)	6	400	-21.2540	-3.335
+S	12	4,000	-21.2635	-3.349
+SD	12	15,700	-21.2652	-3.356
+SDT	12	32,700	-21.2653	-3.356
RASCI wavefunctions				
RAS(3, 1)	12	2,082	-21.2631	-3.343
RAS(3, 2)	12	5,340	-21.2648	-3.350
RAS(4, 2)	12	11,955	-21.2652	-3.355
RAS(4, 3)	12	20,455	-21.2653	-3.356
CAS(12)	12	48,400	-21.2653	-3.356

places, respectively. The higher accuracy is achieved at the expense of higher computational cost, as shown in the steep increase of the CI dimension in table I. The question is then how fast, with respect to the level of approximation within each class of methods, the adequate accuracy is obtained for a given physical problem.

In the following three subsections, we address this question for the description of intense-field driven multielectron dynamics. For this purpose, we consider the temporal evolution of the dipole moment as a basic measure of the accuracy. The high-harmonic generation (HHG) spectrum is investigated in Sec. V D to see the performance of methods to predict an experimentally relevant observable. Appendix D includes numerical test of more complex ORMAS wavefunction than those assessed in this section, addressing a difficulty encountered in propagating such a complex wavefunction. We consider a laser field of the following form;

$$E(t) = E_0 \sin(\omega_0 t) \sin^2\left(\pi \frac{t}{\tau}\right), \quad 0 \leq t \leq \tau. \quad (67)$$

with laser parameters corresponding to a wavelength of 750 nm (period $T \approx 2.5$ fs), a peak intensity of 4×10^{14} W/cm 2 , and a duration of three optical cycles ($\tau = 3T \approx 7.5$ fs).

A. Hartree-Fock reference CI wavefunctions

First we assess the HF+X methods. The ORMAS parameters for the (LiH) $_m$ models are set as $G = 2$, $\mathbf{n} = (N_A/2, 3N_A/2)$, $\mathbf{N}_{\text{min}} = (L, 0)$, and $\mathbf{N}_{\text{max}} = (N_A, L)$, with

$N_A = 2m$, generating following CI spaces;

$$P_{\text{LiH}} = \sum_{l=0}^L [\phi_1]^{2-l} \left[\phi_2 \phi_3 \phi_4 \right]^l, \quad (68a)$$

$$P_{(\text{LiH})_2} = \sum_{l=0}^L [\phi_1 \phi_2]^{4-l} \left[\phi_3 \phi_4 \phi_5 \phi_8 \right]^l, \quad (68b)$$

$$P_{(\text{LiH})_3} = \sum_{l=0}^L [\phi_1 \phi_2 \phi_3]^{6-l} \left[\phi_4 \phi_5 \phi_6 \phi_7 \phi_{12} \right]^l. \quad (68c)$$

We exceptionally set $\mathbf{n} = (N_A/2, N_A/2)$ for the HF+S method [doubly underlined orbitals are removed in Eqs. (68)], for which only $n_A \leq N_A$ is meaningful [39]. This class of methods has been proposed and assessed for 1D models of helium, beryllium, and carbon atoms in Ref. [25]. These models are similar to our 1D-(LiH) $_m$ models with $m = 1, 2, 3$ in the sense that helium, beryllium, and carbon atoms are two, four, and six electron systems, respectively. However, since the inner most orbitals of 1D beryllium and carbon models are energetically far apart from the other orbitals [25], they indeed represent effective two (helium), two (beryllium), and four (carbon) electron problems under the investigated laser parameters [25]. In contrast, our 1D-(LiH) $_m$ models involve *equally important* $N_A = 2m$ active electrons as shown in Fig. 2, thus serve as more stringent test cases.

Figure 3 shows the evolution of the dipole moment computed with HF and HF+X methods. The HF method gives the dipole with large deviations from that of CAS($2N_A$) for all $m = 1, 2, 3$. The HF+X methods with $L \geq 2$ offer a substantially better description, showing the steady convergence to the CAS($2N_A$) description with increasing L . However it should be noted that the convergence rate with respect to L gets slower for larger systems. For example, the HF+SD method ($L = 2$) is exact (equivalent to the CAS) for LiH with $N_A = 2$ [Fig. 3 (a)], closely reproduces the CAS($2N_A$) result for (LiH) $_2$ with $N_A = 4$, except a small deviation at the final stage of the pulse [Fig. 3 (b)], but gives the dipole which noticeably deviates from the CAS($2N_A$) result for (LiH) $_3$ with $N_A = 6$ [Fig. 3 (c)]. We also note that a larger value of L is required to properly describe dynamics than the static electronic structure; the HF+SD describes the ground state of (LiH) $_3$ very well as seen in the inset of Fig. 3 (c), but the accuracy gets deteriorated in the presence the electron-laser interaction. Meanwhile, we observe that the HF+S method gives a reasonably accurate result only for LiH, but brings no major improvement over the HF description for larger systems. This is in contrast to Ref. [39] which reported a good performance of this method for 1D model atoms.

The distinct advantage of the HF+X method, with a fixed L , is the polynomial scaling of the computational cost against N_A , as emphasized in Ref. [25]. However as noted above, the accuracy of the HF+X with a fixed L rapidly drops for larger systems, and depends on the electronic structure in hand. The first difficulty (size dependence) is the consequence of the lack of the size-extensivity [40, 41]. The latter problem (situation dependence) is related to the fundamental limitation of the Hartree-Fock wavefunction; the closed-shell wave-

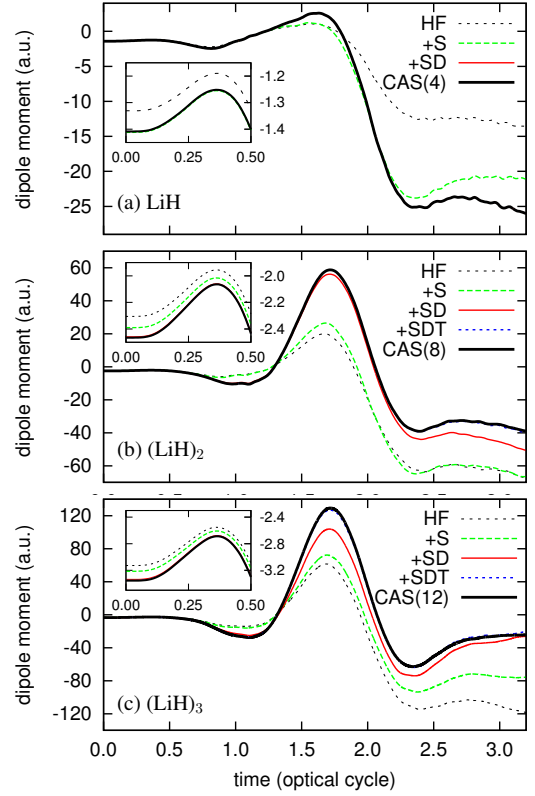


FIG. 3. The time evolution of the dipole moment of (a) LiH, (b) (LiH) $_2$, and (c) (LiH) $_3$ models, computed with HF and HF+X methods (with X=S, SD, SDT signifying $L = 1, 2, 3$, respectively) compared with the CAS($2N_A$) results.

function cannot properly describe tunneling ionization process [23, 38]. The Hartree-Fock reference determinant, in the HF+X method, is no longer a good starting point, demanding the inclusion of higher excitations to describe the more delocalized wavefunction that arises during the course of tunneling ionization.

B. CAS(N_A) reference CI wavefunctions

Next we consider the CAS(N_A)+X methods. The ORMAS parameters are identical to those of the HF+X methods except for the different allocation of $n_A = 2N_A$ active orbitals as $\mathbf{n} = (N_A, N_A)$. The resultant CI spaces for (LiH) $_m$ models with $m = 2, 3$ read

$$P_{(\text{LiH})_2} = \sum_{l=0}^L [\phi_1 - \phi_4]^{4-l} [\phi_5 - \phi_8]^l, \quad (69a)$$

$$P_{(\text{LiH})_3} = \sum_{l=0}^L [\phi_1 - \phi_6]^{6-l} [\phi_7 - \phi_{12}]^l, \quad (69b)$$

This class of methods has been proposed in Ref. [25], but not numerically investigated. We do not show results for LiH, since no new approximations can be generated in the case of $N_A = 2$. One expects that the CAS(N_A) reference serves as

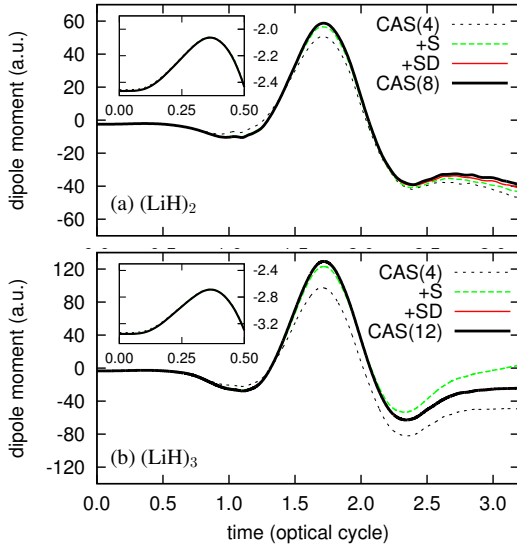


FIG. 4. The time evolution of the dipole moment of (a) $(\text{LiH})_2$, and (b) $(\text{LiH})_3$ models, computed with $\text{CAS}(N_A)$ and $\text{CAS}(N_A)+X$ methods (with $X=S, SD$ signifying $L = 1, 2$, respectively) compared with the $\text{CAS}(2N_A)$ results.

better starting point than the single HF reference in the HF+X method, thus remedies the undesirable system dependence of the accuracy of the latter approach.

This expectation is verified in Fig. 4, which compares the $\text{CAS}(N_A)$ and $\text{CAS}(N_A)+X$ dipoles with the $\text{CAS}(2N_A)$ ones for $(\text{LiH})_2$ and $(\text{LiH})_3$. As seen in the figure, both for $(\text{LiH})_2$ and $(\text{LiH})_3$, the $\text{CAS}(N_A)$ dipole shows much better agreement with the $\text{CAS}(2N_A)$ result than does the HF one (Fig. 3), although the large-amplitude oscillation during the second laser cycle is not completely followed. The $\text{CAS}(N_A)+SD$ method gives the dipoles with excellent agreement with those of $\text{CAS}(2N_A)$, and even the $\text{CAS}(N_A)+S$ method also reproduces the $\text{CAS}(2N_A)$ results surprisingly well.

The reduced system dependence, thus the more uniform accuracy, which is not much affected by different system sizes and different stages of the electron-laser interaction, is achieved by accounting for the most important part of the electron correlation with small CAS expansion (N_A orbitals for N_A electrons), which enables the *remaining* correlation to be included with low rank excitations. In the present case, the first kind of correlation is the breakdown of the closed-shell dominance during the course of tunneling ionization [38]. This is analogous to the *static* correlation involved in the bond breaking process [40, 41]. Although the size-extensivity is still missing in the $\text{CAS}(N_A)+X$ method, the resultant error is considerably reduced from that in the HF+X approach. The drawback is the greater number of determinants involved compared to the HF+X method with the same L , as shown in table I for the $(\text{LiH})_3$ case. The cost scales exponentially with respect to N_A , as just so does the $\text{CAS}(2N_A)$ method.

C. RAS CI wavefunctions

To pursue further flexibility, we consider the RASCI space mentioned in Sec. II B. We set $G = 3$ and $\mathbf{n} = (N_A/2, N_A/2, N_A)$ with $N_A = 2m$. The CI spaces for $(\text{LiH})_2$ and $(\text{LiH})_3$ can be written as

$$P_{(\text{LiH})_2} = \sum_{l_2=0}^{M_{\text{elec}}} \left\{ \sum_{l_1=0}^{M_{\text{hole}}} [\phi_1 \phi_2]^{N_A-l_1} [\phi_3 \phi_4]^{l_1-l_2} \right\} [\phi_5-\phi_8]^{l_2}, \quad (70a)$$

$$P_{(\text{LiH})_3} = \sum_{l_2=0}^{M_{\text{elec}}} \left\{ \sum_{l_1=0}^{M_{\text{hole}}} [\phi_1-\phi_3]^{N_A-l_1} [\phi_4-\phi_6]^{l_1-l_2} \right\} [\phi_7-\phi_{12}]^{l_2}. \quad (70b)$$

The factor within the braces in Eqs. (70), with $l_2 = 0$, represents the CI space with the HF determinant ($l_1 = 0$) plus up to M_{hole} -fold excitations ($l_1 > 0$) to the second subgroup. It serves as the reference CI space, from which further excitations ($l_2 > 0$) to the third subgroup are to be included. Note that if $M_{\text{hole}} = M_{\text{elec}}$, Eqs. (70) reduce to Eqs. (68), while if $M_{\text{hole}} = N_A > M_{\text{elec}}$, Eqs. (70) are identical to Eqs. (69), with $L = M_{\text{elec}}$. In this way, the present RAS scheme provides a flexible series of approximations that includes the HF+X and $\text{CAS}(N_A)+X$ approaches as special cases, with two accuracy (cost) controlling parameters M_{hole} and M_{elec} . See Fig. 1 (d) for a pictorial understanding.

To estimate a reasonable value of M_{hole} , we performed preliminary calculations (not shown) with $M_{\text{elec}} = 0$. They correspond to the HF+X calculations with the active space reduced by half from that in Sec. V A; $\mathbf{n} = (N_A/2, N_A/2)$. We have found that the (reduced) HF+SD and HF+SDT methods approximate the $\text{CAS}(N_A)$ method quite well for $(\text{LiH})_2$ and $(\text{LiH})_3$, respectively, exactly as seen for the twice larger active space in Sec. V A. Thus we use $M_{\text{hole}} = N_A/2 = m$, or more, for $(\text{LiH})_m$. In addition, we consider two possibilities $M_{\text{elec}} = 1, 2$, having the good performance of $\text{CAS}(N_A)+X$ methods with $L = 1, 2$ in mind. For brevity, the method based on Eqs. (70) is denoted as $\text{RAS}(M_{\text{hole}}, M_{\text{elec}})$. The $\text{RAS}(N_A/2, 1)$ and $\text{RAS}(N_A/2, 2)$ methods are further abbreviated as RAS1 and RAS2, respectively, which aim for reduced-cost alternatives to $\text{CAS}(N_A)+S$ and $\text{CAS}(N_A)+SD$ methods, respectively.

Figure 5 shows the dipole moment computed with the RAS1 and RAS2 methods for $(\text{LiH})_2$ and $(\text{LiH})_3$ models. As seen in the figure, these methods closely reproduce the dipole evolution of the $\text{CAS}(2N_A)$ method, including the global oscillation at the center of the pulse. In closer look at the figure, the RAS1 dipole evolutions are found to be very similar to those of the $\text{CAS}(N_A)+S$ method in Fig. 4. The RAS2 result of $(\text{LiH})_2$ is identical to that of HF+SD in Fig. 3, as should be so since $M_{\text{hole}} = M_{\text{elec}}$. In whole, the performance of the RAS methods is satisfactory especially when we notice the significant reduction of the CI dimension as shown in table I for $(\text{LiH})_3$. We further confirmed (not shown) that increasing M_{hole} by one ($M_{\text{hole}} = N_A/2 + 1 = m + 1$) results in the dipole which is indistinguishable, in the scale of the figure, from the corresponding $\text{CAS}(N_A)+X$ one. The high per-

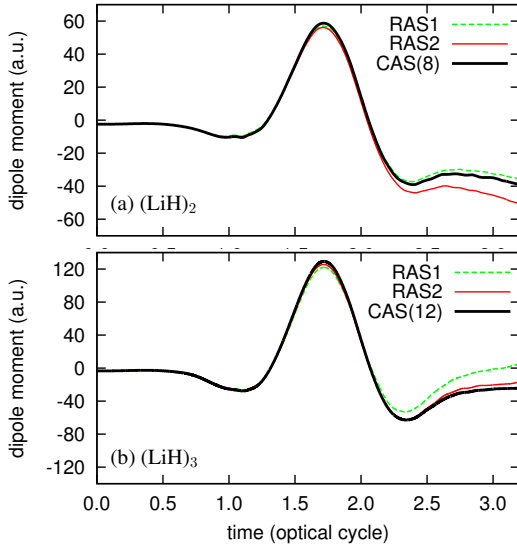


FIG. 5. The time evolution of the dipole moment of (a) $(\text{LiH})_2$, and (b) $(\text{LiH})_3$ models, computed with RAS1 and RAS2 methods compared with the $\text{CAS}(2N_A)$ results.

formance of the RAS schemes is attributed to the two-stage approximations controlled by M_{hole} and M_{elec} ; The reference CI space accounts for the (system-dependent) important part of the correlation (with system-dependent M_{hole}), while the excited configurations are responsible for the remaining part (with M_{elec} typically up to doubles).

D. High-harmonic generation spectrum

Next we investigate HHG spectra. The HHG spectrum is obtained by the Fourier transform of the expectation value of the dipole acceleration evaluated using the Ehrenfest expression [42]. Before entering the assessment of different methods, we comment on the physical interpretation of the HHG spectra of $(\text{LiH})_m$ models. Figure 6 shows the HHG spectra computed with the $\text{CAS}(2N_A)$ methods. Shown in the figure with downward arrows are the cutoff positions, calculated based on the static Hartree-Fock-Koopmans picture;

$$\omega_i^{\text{cutoff}} = -\epsilon_i + 3.17U_p, \quad (71)$$

where $U_p \equiv E_0^2/4\omega_0^2$ is the ponderomotive energy, and ϵ_i is the orbital energy depicted in Fig. 2. As seen in Fig. 6 (a), the computed HHG spectrum of LiH is characterized by the two-stage cutoff structure, with the positions of the first and second cutoff being well reproduced by Eq. (71) with weakly (I) and

deeply (II) bound orbital energies, respectively. The comparison of dynamical-core and frozen-core treatments [denoted as $\text{CAS}(2N_A)$ and $\text{CAS}(2N_A)\text{-FC}$, respectively] reveals that the second cutoff originates from the core response, since it is absent in the frozen-core spectrum. This simple picture based on the independent particle model gets less valid in larger systems [Fig. 7 (b) and (c)]. The higher complexity of the spectra for larger systems is presumably attributed to the higher probability of multiple ionizations and the increasing importance of the multichannel effect with growing molecular size. Further physical discussions of HHG spectra will be made elsewhere. Below we focus on how the various methods reproduce the $\text{CAS}(2N_A)$ spectra.

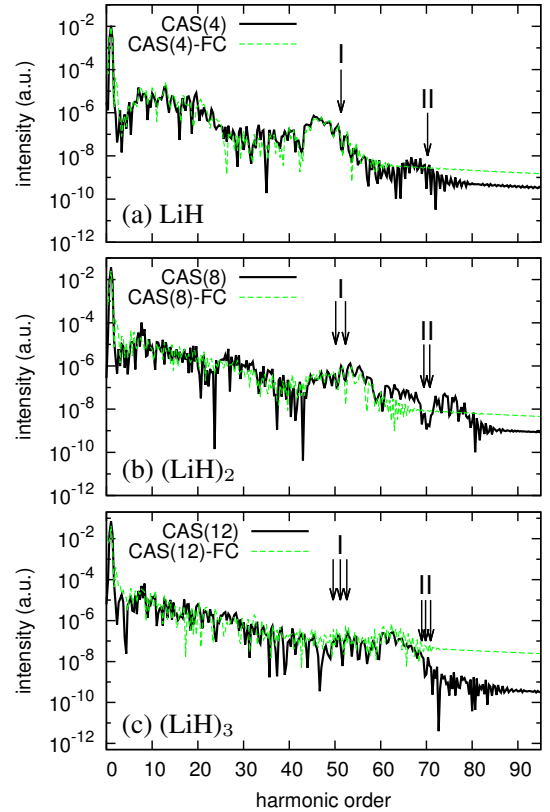


FIG. 6. The HHG spectra of (a) LiH, (b) $(\text{LiH})_2$, and (c) $(\text{LiH})_3$ models, exposed to a laser pulse of the form Eq. (67) with a wavelength of 750 nm and an intensity of $4 \times 10^{14} \text{ W/cm}^2$, computed with $\text{CAS}(2N_A)$ methods. The dynamical-core and frozen-core (“FC” appended) spectra are compared. The three-step model prediction of cutoff positions are indicated by arrows. See text for more details.

Figure 7 compares the HHG spectra computed with HF and HF+X methods with those of $\text{CAS}(2N_A)$. As can be seen in Fig. 7 (a), the HF method already gives the HHG spectrum of LiH with a good agreement with that of $\text{CAS}(4)$, as opposed to

the large deviation in the dipole moment [Fig. 3 (a)]. With the present laser setting, the high-harmonic emissions are dominated by those during the second laser cycle ($T < t < 2T$). As seen in Fig. 3 (a), for LiH, the electron motion within

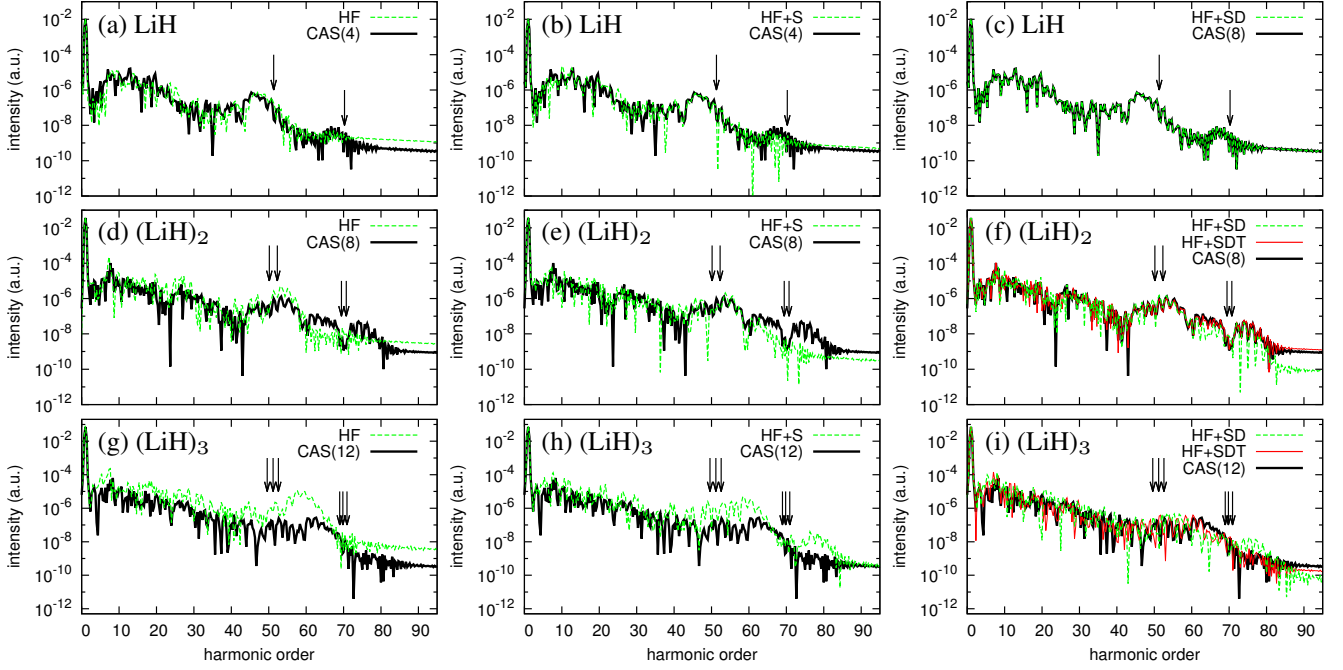


FIG. 7. The HHG spectra of LiH (a-c), $(\text{LiH})_2$ (d-f), and $(\text{LiH})_3$ (g-i) models, computed with HF and HF+X methods (with X=S, SD, SDT signifying $L = 1, 2, 3$, respectively) compared with $\text{CAS}(2N_A)$ spectra. Also see the caption of Fig. 6.

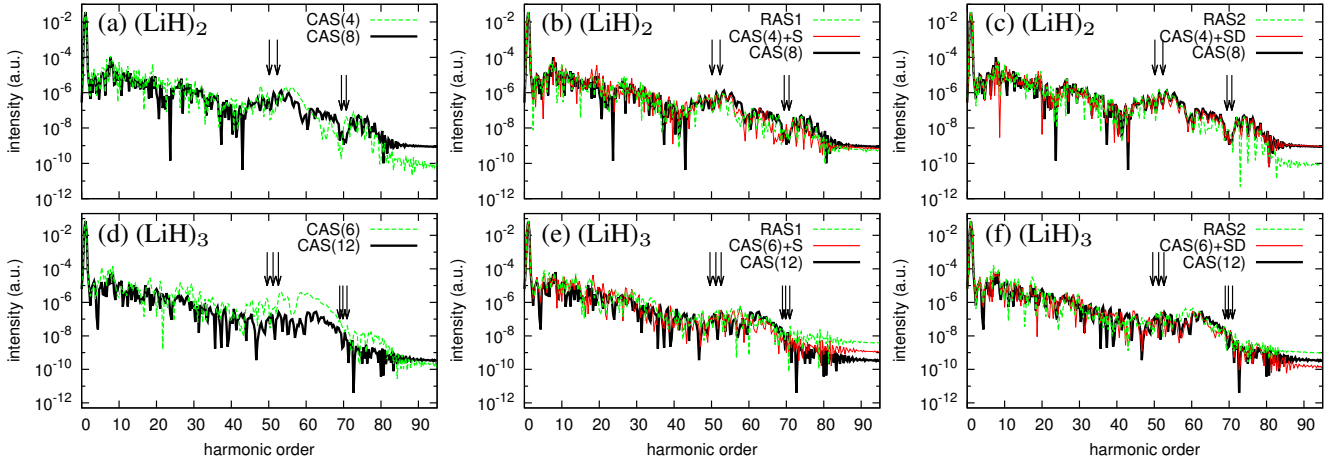


FIG. 8. The HHG spectra of $(\text{LiH})_2$ (a-c), and $(\text{LiH})_3$ (d-f) models, computed with $\text{CAS}(N_A)$, $\text{CAS}(N_A)+X$ (with X=S, SD signifying $L = 1, 2$, respectively) and RAS methods compared with $\text{CAS}(2N_A)$ spectra. Also see the caption of Fig. 6.

this time region is restricted near the origin, which allows the HF method for a qualitatively correct description. In contrast, for $(\text{LiH})_2$ and $(\text{LiH})_3$, the HF method clearly overestimates the spectral intensity below the first cutoff. The underestimation of tunneling ionization and first-order response, and the overestimation of harmonic intensity for a high-intensity laser are common faults of the TDHF method [23, 34, 37, 38, 43]. The argument for the performance of the HF+X methods goes parallel to that for the dipole moment made in Sec. V A; Increasing L steadily improves the description, but the accuracy with a fixed L gets poorer for larger systems. The HF+SDT method well reproduces the $\text{CAS}(2N_A)$ spectra up to $(\text{LiH})_3$.

The HF+SD and $\text{CAS}(2N_A)$ spectra agree exactly and quite well for LiH and $(\text{LiH})_2$, respectively, but deviates noticeably for $(\text{LiH})_3$. The HF+S spectrum of $(\text{LiH})_3$ is no better than that of the HF method.

The HHG spectra computed with $\text{CAS}(N_A)$, $\text{CAS}(N_A)+X$, and RAS methods are shown in Fig. 8. The performance of the $\text{CAS}(N_A)$ method [Fig. 8 (a) and (d)] is found unsatisfactory, with little improvement over the HF spectra [Fig. 7 (d) and (g)]. However, as in Figs. 8 (c) and (f), the $\text{CAS}(N_A)+\text{SD}$ spectra show a quite good agreement with the $\text{CAS}(2N_A)$ ones. This convinces us that the $\text{CAS}(N_A)$ description is indeed the adequate starting point (qualitatively correct for the

tunneling ionization event), on top of which the remaining correlation effect is included effectively with low rank excitations. It is encouraging that the $\text{CAS}(N_A)+\text{S}$ method also gives rather accurate HHG spectra as shown in Figs. 8 (b) and (e). Finally, as in the case of dipole evolution, the RAS1 and RAS2 methods perform similarly to the $\text{CAS}(N_A)+\text{S}$ and $\text{CAS}(N_A)+\text{SD}$ methods, respectively, despite their significantly reduced CI dimensions. Again, we confirmed (not shown) that the HHG spectrum of $(\text{LiH})_3$ computed with the RAS(4, 2) method [with M_{hole} increased by one from the RAS2 \equiv RAS(3, 2) method] agrees almost perfectly with that of the $\text{CAS}(N_A)+\text{SD}$ method. The great advantage of the $\text{CAS}(N_A)+\text{X}$ and RAS methods is that the accuracy with a fixed L (M_{elec}) is not lost for larger systems as badly as in the case of the HF+X method.

E. Analyses of computational cost

Finally we analyze the computational cost of the TD-ORMAS methods using the simulation for $(\text{LiH})_3$ as an example. Table II shows CPU times for propagating 1000 time steps from the initial ground-state with various methods using the algorithm described in Sec. IV, recorded on a single Xeon processor with a clock frequency of 3.33 GHz. It is encouraging that the HF+SDT, CAS(6)+S, CAS(6)+SD, RAS(3, 1), and RAS(3, 2) methods, which are reasonably accurate for $(\text{LiH})_3$ as shown in Secs. V A-V D, all reduce the total computational time compared to that of the CAS(12) method, with relative speed-up factors 2.3, 4.5, 2.0, 4.7, and 2.6, respectively. Table II also shows the CPU times for the computational steps (1)+(5), (2)–(4), and (7) described in Sec. IV, separately. Their sum accounts for more than 98% of the total CPU time. As seen in the table, the CPU times for steps (1)+(5) are reduced for the case of approximate methods depending on the number of determinants N_{det} , while those of

steps (2)–(4) are roughly constant [except for CAS(6)+S and RAS(3, 1) methods, mentioned shortly]. This is because the former step (RDMs and CI derivatives) scales linearly with N_{det} , while the latter (orbital derivatives except for the active-active terms and operator integrals) is independent of N_{det} , and depends only on the number of orbitals and basis functions or grid points [23].

The CPU times for steps (2)–(4) of CAS(6)+S and RAS(3, 1) methods are shorter than those of the other methods. This is due to the higher sparsity of the 2RDM [originating, in turn, from the maximum occupancy 1 of the last orbital subgroup as shown in Fig. 1 (c) and (d)], which reduces the cost for the second term of Eq. (39b). Also, the sparsity of the coupling coefficients of these methods makes the steps (1)+(5) faster. Consequently, the total CPU times of CAS(6)+S and RAS(3, 1) methods are shorter than that of the HF+SD method despite their larger N_{det} as shown in table I. Finally, the step (7), which is unique to the method with a non-complete CI space, is found to occupy less than 1% of the total CPU time, highlighting the high efficiency of the algorithm given in Appendix A. As a whole, the flexibility of the TD-ORMAS method and its optimal implementation enable computational cost reduction without significant loss of accuracy.

VI. SUMMARY

A new time-dependent multiconfiguration method is developed based on the ORMAS scheme to construct non-complete CI spaces. The TD-ORMAS method attains further flexibility on top of the previously developed TD-CASSCF method [23] by the subdivision of active orbitals into an arbitrary number of subgroups and the occupation restriction posed for each subgroup of orbitals. The equations of motion for the CI coefficients and orbital functions in the TD-ORMAS method, derived based on the time-dependent variational principle, are shown to be formally identical to those of the TD-CASSCF method, except for the non-vanishing active inter-group terms of orbital time derivatives. An efficient algorithm is devised to solve for the inter-group contributions, circumventing the costly evaluation of the three-particle reduced density matrix. The core wavefunction is explicitly separated from the active CI space [Eq. (11)], transforming the original N -electron CI equation [Eq. (32)] to that of N_A active electrons [Eq. (48)]. The implementation of the TD-ORMAS method is described in depth, allowing existent MCTDHF codes to be readily adapted to the TD-ORMAS method.

Out of a variety of methods that fall within the TD-ORMAS framework, several representative classes of methods are studied in detail; the HF+X, $\text{CAS}(N_A)+\text{X}$, and RAS methods. Note that the present RAS method is the straightforward time-dependent version of the stationary RASSCF method, differently from the “TD-RASSCF” method of Ref. [25] (See Sec. II B). All the investigated approaches provide a systematic series of approximations that converge to the TD-CASSCF description, but at different rates with respect to the level of approximation [the value(s) of L , or M_{hole} and M_{elec}].

TABLE II. Computational times for the 1D- $(\text{LiH})_3$ model. The CPU times (second) for the computational steps (1)+(5), (2)–(4), and (7) of Sec. IV as well as the total CPU time are shown for various methods. The total speed-up factor relative to the CAS(12) method are also shown in parentheses. See text for more details.

Method	(1)+(5)	(2)–(4)	(7)	Total	
HF reference CI wavefunctions					
HF+SD	196.6	688.2	3.7	898.2	(3.8)
+SDT	780.7	678.5	12.7	1481.1	(2.3)
+SDTQ	1565.6	676.9	13.8	2265.9	(1.5)
CAS(6) reference CI wavefunctions					
CAS(6)+S	202.9	551.2	2.2	766.0	(4.5)
+SD	1041.5	680.0	9.9	1741.1	(2.0)
+SDT	1991.3	690.5	14.9	2706.4	(1.3)
RASCI wavefunctions					
RAS(3, 1)	157.2	556.4	2.8	726.6	(4.7)
RAS(3, 2)	603.4	684.6	10.3	1308.5	(2.6)
RAS(4, 2)	905.5	683.8	11.2	1610.9	(2.1)
RAS(4, 3)	1456.2	686.9	15.8	2169.1	(1.6)
CAS(12)	2736.5	689.8	0.0	3434.9	

Among these methods, the present numerical analyses highlight the RAS method (encompassing the former two as special cases) as the most cost effective one, which allows the separate calibrations for the reference CI space (by varying M_{hole}) and for the further excitations from the reference (by varying M_{elec}), thus enabling more flexible convergence studies and applications with a reliable accuracy. We plan to make further assessment of above-mentioned and other problem-specific TD-ORMAS methods based on three-dimensional implementation. This article has worked out the theoretical issues regarding the use of non-complete CI spaces, and provides a solid ground for more realistic applications.

ACKNOWLEDGMENTS

We thank Dr. H. Miyagi and Dr. L. B. Madsen in Aarhus University for discussions. This research is supported in part by Grant-in-Aid for Scientific Research (No. 23750007, 23656043, 23104708, 25286064, 26390076, and 26600111) from the Ministry of Education, Culture, Sports, Science and Technology (MEXT) of Japan, and also by Advanced Photon Science Alliance (APSA) project commissioned by MEXT. This research is also partially supported by the Center of Innovation Program from Japan Science and Technology Agency, JST.

Appendix A: Evaluation of matrix elements of Eqs. (58)-(61)

To compute the matrix elements of Eqs. (58)-(61), we first evaluate the following quantities;

$$\bar{P}_{tv}^{uw} = \langle \Psi_A | \hat{E}_u^t \hat{Q} \hat{E}_v^w | \Psi_A \rangle, \quad (\text{A1})$$

$$\bar{B}_t^u = \langle \Psi_A | \hat{E}_u^t \hat{Q} \hat{H}_A - \hat{H}_A \hat{Q} \hat{E}_u^t | \Psi_A \rangle, \quad (\text{A2})$$

from which \mathbf{A} and \mathbf{b} are easily obtained. First, the tensor \bar{P} is obtained as a by-product in computing the 2RDM, since

$$\begin{aligned} P_{tv}^{uw} &= \langle \Psi_A | E_u^t E_w^v - E_w^t E_u^v | \Psi_A \rangle \\ &= \langle \Psi_A | E_u^t (\hat{P} + \hat{Q}) E_w^v - E_w^t E_u^v | \Psi_A \rangle \\ &= \langle \Psi_A | E_u^t \hat{P} E_w^v | \Psi_A \rangle + \bar{P}_{tv}^{uw} - D_t^w \delta_v^u, \end{aligned} \quad (\text{A3})$$

where the identities $\hat{E}_{uv}^{tv} = \hat{E}_u^t \hat{E}_v^v - \hat{E}_w^t \delta_u^v$ and $\hat{P} + \hat{Q} = \hat{1}$ are used. Next, the \bar{B} matrix is computed as follows;

$$\begin{aligned} \bar{B}_t^u &= \langle \Psi_A | \hat{E}_u^t (\hat{1} - \hat{P}) \hat{H}_A - \hat{H}_A (\hat{1} - \hat{P}) \hat{E}_u^t | \Psi_A \rangle \\ &= \langle \Psi_A | [\hat{E}_u^t, \hat{H}_A] | \Psi_A \rangle - \langle \Psi_A | \hat{E}_u^t \hat{P} \hat{H}_A - \hat{H}_A \hat{P} \hat{E}_u^t | \Psi_A \rangle \\ &= B_t^u - (D_t'^u - D_u'^{t*}), \end{aligned} \quad (\text{A4})$$

where Eq. (45) is used, and $D_t'^u \equiv \langle \Psi_A | \hat{E}_u^t | \Psi_A' \rangle$, with

$$| \Psi_A' \rangle = \sum_{\mathbf{I}} |\mathbf{I}\rangle C_{\mathbf{I}}', \quad C_{\mathbf{I}}' = \langle \mathbf{I} | \hat{H}_A | \Psi_A \rangle. \quad (\text{A5})$$

The transformed coefficient $C_{\mathbf{I}}'$ in Eq. (A5) is a part of the CI derivative (48) obtained beforehand in the step (5) of Sec. IV,

and the 1RDM like matrix D' is easily computed with a cost typically an order of magnitude smaller than that of 2RDM. As a consequence, \bar{P} and \bar{B} (therefore \mathbf{A} and \mathbf{b}) can be obtained with a small additional effort on top of all the other operations.

Reference [25] took a different approach, involving the explicit computation of a part of the third-order reduced density matrix,

$$\zeta_{tvx}^{uwy} \equiv \langle \Psi_A | \hat{E}_u^t \hat{Q} \hat{E}_{wy}^{vx} | \Psi_A \rangle, \quad (\text{A6})$$

to evaluate the two electron contributions to Eq. (A2) as

$$\langle \Psi_A | \hat{E}_u^t \hat{Q} \hat{H}_A | \Psi_A \rangle \leftarrow \frac{1}{2} \sum_{vwxy} g_{wy}^{vx} \zeta_{tvx}^{uwy}. \quad (\text{A7})$$

This constitutes a sever computational bottleneck, thus hampers the inclusion of high rank excitations ($L > 3$) in the case of large active spaces. The present algorithm [Eqs. (A4)-(A5)] removes this bottleneck.

Appendix B: Active inter-group contributions for RASSCF wavefunction

Equation (57) can be transformed into a simpler form in case of the RASSCF wavefunction [28]. As noted in Ref. [28] for the RASCI space, while upward *excitations* $E_u^t | \Psi_A \rangle$ ($t > u$) can create states lying across P and Q spaces, all *deexcited* configurations $E_t^u | \Psi_A \rangle$ ($t > u$) belong to the P space or vanish. Using this fact in Eqs. (58)-(61) leads

$$\sum_{v>w}' A_{tu,vw}^{\text{RAS}} X_{vw} = \mathbf{b}_{tu}^{\text{RAS}}, \quad (\text{B1})$$

where

$$\mathbf{A}_{tu,vw}^{\text{RAS}} \equiv \langle \Psi_A | \hat{E}_t^u \hat{Q} \hat{E}_w^v | \Psi_A \rangle, \quad (\text{B2})$$

$$\mathbf{b}_{tu}^{\text{RAS}} \equiv \langle \Psi_A | \hat{E}_t^u \hat{Q} \hat{H}_A | \Psi_A \rangle. \quad (\text{B3})$$

This is identical to the equation used in Ref. [25]. Since the matrix equation (B1) has the same dimension as the general equation (57) (solution vector consists of two times N_{tot} real values), we chose to always solve Eq. (57).

Appendix C: Imaginary time propagation

Appropriate equations for the imaginary time propagation can be derived from the action integral (24) defined across the pure imaginary time axis $t = -i\tau$ with a real variable τ . Noting the following dual correspondence;

$$| \frac{\partial \Psi}{\partial t} \rangle = i | \frac{\partial \Psi}{\partial \tau} \rangle \leftrightarrow \langle \frac{\partial \Psi}{\partial t} | = -i \langle \frac{\partial \Psi}{\partial \tau} |, \quad (\text{C1})$$

the imaginary time counterpart of Eq. (25) is obtained as

$$\delta S = \delta \langle \Psi | \hat{H} | \Psi \rangle + \left(\langle \delta \Psi | \frac{\partial \Psi}{\partial \tau} \rangle + \langle \frac{\partial \Psi}{\partial \tau} | \delta \Psi \rangle \right). \quad (\text{C2})$$

Based on this expression, formally the same equations are derived for the CI derivative [Eq. (48)], and Q -space and core-active contributions [Eqs. (37) and (43)] to the orbital derivative, except for a replacement $-i \rightarrow -1$ in the first term of these equations. One should take into account the sign difference of the third term of Eqs. (25) and (C2) for active intergroup rotations, in general. This results in the equation identical to Eq. (57) with the coefficient matrix of Eqs. (58) and (59) redefined as follows;

$$A_{tu,vw}^{\mp\mp} = \pm \text{Re} \langle \Psi_A | \hat{E}_{tu}^{\mp} \hat{Q} \hat{E}_{vw}^{\mp} | \Psi_A \rangle, \quad (\text{C3})$$

$$A_{tu,vw}^{\mp\pm} = \pm \text{Im} \langle \Psi_A | \hat{E}_{tu}^{\mp} \hat{Q} \hat{E}_{vw}^{\pm} | \Psi_A \rangle, \quad (\text{C4})$$

constituting the real symmetric linear system of equations. If both CI coefficients and orbitals are represented by real numbers (as for the non-degenerate ground state without external magnetic field), variations and time derivatives of orbitals are parameterized only with real anti-symmetric part of Eqs. (52) and (53), leading a matrix equation with half the dimension of Eq. (57);

$$\sum_{v>w}' \langle \Psi_A | \hat{E}_{tu}^{\mp} \hat{Q} \hat{E}_{vw}^{\mp} | \Psi_A \rangle X_{vw}^R = - \langle \Psi_A | \hat{E}_{tu}^{\mp} \hat{Q} \hat{H}_A | \Psi_A \rangle. \quad (\text{C5})$$

Appendix D: Test of more complex ORMAS wavefunction

All the simulations adopting the non-complete CI spaces presented in Sec. V have no stability problem; the integration of the EOMs is found to be as stable as that of the CAS method. Here we give an example of the difficult case. We set $G = 3$, $\mathbf{n} = (1, 1, 6)$, $\mathbf{N}_{\min} = (1, 1, 0)$, and $\mathbf{N}_{\max} = (2, 2, 2)$, generating the following CI space for $(\text{LiH})_2$:

$$P = \sum_{l_1=0}^1 \sum_{l_2=0}^1 [\phi_1]^{2-l_1} [\phi_2]^{2-l_2} [\phi_3-\phi_8]^{l_1+l_2}. \quad (\text{D1})$$

Figure 9 shows the evolution of the dipole computed using this CI space. Unlike the simulations in Sec. V, we had to use a step size control to complete the simulation, with significantly larger values ($\delta \geq 10^{-4}$) for the regularization parameter. The figure reveals the δ dependence of the computed

dipoles; although the result with $\delta^2 = 10^{-8}$ seems to be near the convergence, the simulation with $\delta^2 = 10^{-9}$ ends up with the divergence at around $t = 1.63T$. This problem arises due to the near singularity of the coefficient matrix A in Eq. (65), with the smallest singular value of A dropping below 10^{-7} at the divergence point. Generally, the occurrence of the stability problem is the sign that the chosen CI space is not appropriate for the problem in hand. In the present case, the CI space should be revised as $P \rightarrow P' = P + \Delta P$ with

$$\Delta P = \{ [\phi_1]^2 [\phi_2]^0 + [\phi_1]^0 [\phi_2]^2 \} [\phi_3-\phi_8]^2, \quad (\text{D2})$$

which is equivalent to the HF+SD CI space, making the rotation between ϕ_1 and ϕ_2 redundant.

Another view of Fig. 9 is that the dipole obtained with the present method (hopefully nearly convergent with respect to δ) agrees with the CAS(8) result much better than that of the HF+S method given in Fig. 3. Rather the performance is similar to that of the HF+SD method. The CI space of Eq. (D1) can be decomposed as

$$P = P_{\text{HF+S}} + [\phi_1]^1 [\phi_2]^1 [\phi_3-\phi_8]^2, \quad (\text{D3})$$

where $P_{\text{HF+S}}$ is given by Eq. (68a) with $L = 1$ and underlined orbitals included. Then, the aforementioned performance comparison indicates the importance of *product* double excitations represented by the second term of Eq. (D3). This encourages the development of the time-dependent size extensive theory such as the coupled-cluster theory [44].

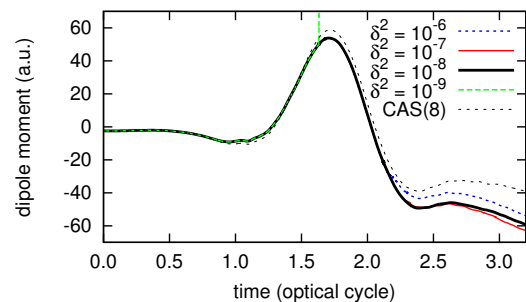


FIG. 9. The time evolution of the dipole moment of $(\text{LiH})_2$ model, obtained using the CI space of Eq. (D1) with different values of δ .

-
- [1] F. Krausz and M. Ivanov, Rev. Mod. Phys. **81**, 163 (2009).
 - [2] M. S. Pindzola and F. Robicheaux, Phys. Rev. A **57**, 318 (1998).
 - [3] M. S. Pindzola and F. Robicheaux, J. Phys. B **31**, L823 (1998).
 - [4] J. Colgan, M. S. Pindzola, and F. Robicheaux, J. Phys. B **34**, L457 (2001).
 - [5] J. S. Parker, L. R. Moore, K. J. Meharg, D. Dundas, and K. T. Taylor, J. Phys. B **34**, L69 (2001).
 - [6] S. Laulan and H. Bachau, Phys. Rev. A **68**, 013409 (2003).
 - [7] B. Piraux, J. Bauer, S. Laulan, and H. Bachau, Eur. Phys. J. D **26**, 7 (2003).
 - [8] S. Laulan and H. Bachau, Phys. Rev. A **69**, 033408 (2004).
 - [9] K. L. Ishikawa and K. Midorikawa, Phys. Rev. A **72**, 013407 (2005).
 - [10] J. Feist, S. Nagele, R. Pazourek, E. Persson, B. I. Schneider, L. A. Collins, and J. Burgdörfer, Phys. Rev. Lett. **103**, 063002 (2009).
 - [11] R. Pazourek, J. Feist, S. Nagele, E. Persson, B. I. Schneider, L. A. Collins, and J. Burgdörfer, Phys. Rev. A **83**, 053418 (2011).
 - [12] K. L. Ishikawa and K. Ueda, Phys. Rev. Lett. **108**, 033003 (2012).
 - [13] S. Sukiasyan, K. L. Ishikawa, and M. Ivanov, Phys. Rev. A **86**, 033423 (2012).
 - [14] K. L. Ishikawa and K. Ueda, Appl. Sci. **3**, 189 (2013).

- [15] W. Vanroose, D. A. Horner, F. Martín, T. N. Rescigno, and C. W. McCurdy, *Phys. Rev. A* **74**, 052702 (2006).
- [16] D. A. Horner, S. Miyabe, T. N. Rescigno, C. W. McCurdy, F. Morales, and F. Martín, *Phys. Rev. Lett.* **101**, 183002 (2008).
- [17] T.-G. Lee, M. S. Pindzola, and F. Robicheaux, *J. Phys. B* **43**, 165601 (2010).
- [18] J. Caillat, J. Zanghellini, M. Kitzler, O. Koch, W. Kreuzer, and A. Scrinzi, *Phys. Rev. A* **71**, 012712 (2005).
- [19] T. Kato and H. Kono, *Chem. Phys. Lett.* **392**, 533 (2004).
- [20] M. Nest, T. Klamroth, and P. Saalfrank, *J. Chem. Phys.* **122**, 124102 (2005).
- [21] D. J. Haxton, K. V. Lawler, and C. W. McCurdy, *Phys. Rev. A* **83**, 063416 (2011).
- [22] D. Hochstuhl and M. Bonitz, *J. Chem. Phys.* **134**, 084106 (2011).
- [23] T. Sato and K. L. Ishikawa, *Phys. Rev. A* **88**, 023402 (2013).
- [24] H. Miyagi and L. B. Madsen, *Phys. Rev. A* **87**, 062511 (2013).
- [25] H. Miyagi and L. B. Madsen, *Phys. Rev. A* **89**, 063416 (2014).
- [26] J. Ivanic, *J. Chem. Phys.* **119**, 9364 (2003).
- [27] J. Ivanic, *J. Chem. Phys.* **119**, 9377 (2003).
- [28] J. Olsen, B. O. Roos, P. Jørgensen, and H. J. A. Jensen, *J. Chem. Phys.* **89**, 2185 (1988).
- [29] R. P. Miranda, A. J. Fisher, L. Stella, and A. P. Horsfield, *J. Chem. Phys.* **134**, 244101 (2011).
- [30] J. Frenkel, *Wave Mechanics-Advanced General Theory* (Oxford at the Clarendon Press, 1934).
- [31] P.-O. Löwdin and P. K. Mukherjee, *Chem. Phys. Lett.* **14**, 1 (1972).
- [32] R. Moccia, *Int. J. Quantum Chem.* **7**, 779 (1973).
- [33] A. I. Panin and K. V. Simon, *Int. J. Quantum Chem.* **59**, 471 (1996).
- [34] M. S. Pindzola, D. C. Griffin, and C. Bottcher, *Phys. Rev. Lett.* **66**, 2305 (1991).
- [35] M. S. Pindzola, F. Robicheaux, and P. Gavras, *Phys. Rev. A* **55**, 1307 (1997).
- [36] N. E. Dahlen and R. van Leeuwen, *Phys. Rev. A* **64**, 023405 (2001).
- [37] N. A. Nguyen and A. D. Bandrauk, *Phys. Rev. A* **73**, 032708 (2006).
- [38] T. Sato and K. L. Ishikawa, *J. Phys. B: At. Mol. Opt. Phys.* **47**, 204031 (2014).
- [39] H. Miyagi and L. B. Madsen, *J. Chem. Phys.* **140**, 164309 (2014).
- [40] A. Szabo and N. S. Ostlund, *Modern Quantum Chemistry* (Dover, Mineola, 1996).
- [41] T. Helgaker, P. Jørgensen, and J. Olsen, *Molecular Electronic-Structure Theory* (Wiley, 2002).
- [42] A. D. Bandrauk, *J. Phys. B: At. Mol. Opt. Phys.* **46**, 153001 (2013).
- [43] K. C. Kulander, K. J. Schafer, and J. L. Krause, in *Atoms in Intense Laser Fields*, edited by M. Gavrilu (Academic Press, New York, 1992) pp. 247–300.
- [44] S. Kvaal, *J. Chem. Phys.* **136**, 194109 (2012).